ORIGINAL PAPER

Spinel structure of activated carbon supported MFe$_2$O$_4$ composites as an economic and efficient electrocatalyst for oxygen reduction reaction in neutral media

Hanaa M. Sabaa[1] · K. M. El-Khatib[2] · Mohamed Y. El-Kady[3] · Sawsan A. Mahmoud[1]

Abstract

For more sustainability and marketing of microbial fuel cells (MFCs) in wastewater treatment, the sluggish kinetics of cathode oxygen reduction reaction (ORR) and platinum scarcity (with its high cost) should be swept away. So, this work aimed to synthesize metal ferrite (MFe$_2$O$_4$; M = Mn, Cu, and Ni) -based activated carbon composites as inexpensive ORR cathode catalysts. The composites were synthesized using a facile modified co-precipitation approach with low-thermal treatment and labeled as MnFe$_2$O$_4$/AC, CuFe$_2$O$_4$/AC, and NiFe$_2$O$_4$/AC. The as-synthesized catalysts are physicochemically characterized by X-ray diffraction (XRD), Raman spectroscopy, Fourier transform infrared microscopy (FTIR), Barrett-Joyner-Halenda (BJH), scanning electron microscopy (SEM), high-resolution transmission electron microscopy (HR-TEM), and electron spin resonance (ESR). The electrochemical catalytic performance toward ORR was studied in a phosphate buffer solution (PBS) at neutral media via cyclic voltammetry (CV) and linear sweep voltammetry (LSV). MnFe$_2$O$_4$/AC has the highest onset potential (E_{onset}) value of -0.223 V compared to CuFe$_2$O$_4$/AC (-0.280 V) and NiFe$_2$O$_4$/AC (-0.270 V). MnFe$_2$O$_4$/AC also has the highest kinetic current density (j_K) and lowest Tafel slope (-5 mA cm^{-2} and -330 mV dec^{-1}) compared to CuFe$_2$O$_4$/AC (-3.05 mA cm^{-2} and -577 mV dec^{-1}) and NiFe$_2$O$_4$/AC (-2.67 mA cm^{-2} and -414 mV dec^{-1}). The ORR catalyzed by MnFe$_2$O$_4$/AC at pH = 7 proceeds via a 4e$^-$ -kinetic pathway. The ESR is in good agreement with the electrochemical analysis due to the highest ΔH_{pp} value for MnFe$_2$O$_4$/AC compared to CuFe$_2$O$_4$/AC and NiFe$_2$O$_4$/AC. Thus, MnFe$_2$O$_4$/AC is suggested as a promising alternative to Pt- electrocatalyst cathode for MFCs at neutral conditions.

Keywords Metal ferrite · MFe$_2$O$_4$ spinel structure · Activated carbon · ESR · Oxygen reduction reaction · Neutral media and microbial fuel cell

Introduction

There is a growing demand to develop clean and renewable energy sources [1]. To meet this energy growth, fuel cells have gained worldwide attention as a green, high-efficiency, and sustainable electrochemical energy conversion device [2]. Among

them, the microbial fuel cell (MFC) as a bio-electrochemical apparatus has gained researchers' interest owing to its capability of directly harvesting electrical energy during the wastewater treatment process [2, 3]. However, the MFCs' widespread application is hindered by the high overpotentials that arise from the sluggish kinetics of the cathode oxygen reduction reaction (ORR) at neutral pH conditions [4, 5]. Although platinum (Pt) is the most efficient and widely used electrocatalyst for ORR, its commercial applicability in fuel cells is limited due to its scarcity and high cost [6]. Thus, developing inexpensive and effective ORR catalysts such as metal-free electrocatalyst [1], non-precious metal (Mn, Co, and Fe)-based catalysts [7], transition metal oxides (TMOs), and metal-nitrogen-carbon (M-N-C) [8] as alternatives that could reduce the dependence on the currently employed Pt, which has become an urgent research area.

✉ Sawsan A. Mahmoud
  sawsanhassan2003@yahoo.com

1   Processes Development Department, Egyptian Petroleum Research Institute, Nasr City, Postal Code 11727, Cairo, Egypt

2   Chemical Engineering & Pilot Plant Department, Engineering Research Institute, National Research Centre, 33 El-Buhouth St, Dokki 12311, Cairo, Egypt

3   Chemistry Department, Faculty of Science, Ain Shams University, Cairo, Egypt

Among these alternatives, TMOs (Fe, Ni, Mn, Cu, etc.) have gained increasing interest as ORR cathode catalysts in MFCs because of their abundance, ease of doping, structural diversity, low cost, high ORR activity, and environmental friendliness [8–10]. However, the TMOs suffer from synthesis uncontrollable growth, high electrical resistance, poor electrical conductivity, and low catalytic activity [11, 12]. Besides, the dissolution and sintering during the fuel cell reactions result in decreasing fuel cells' ORR performance [13]. Combining two or more low-cost TMOs into different spinel structures (MTMOs; mixed transition metal oxides) is a powerful way to boost the ORR activity. Due to its ability to mix well into one material and variable oxidation states [11], good cycle stability [10], low cost, environmental friendliness, and higher electrical conductivity than the simple TMOs [14–16]. Recently, MTMOs with a spinel structure and AB_2O_4 general molecular formula appear as promising ORR electrocatalysts [17].

Spinel-metal ferrites (MFe_2O_4; M = Mn, Ni, Cu, Co, etc.) are one of the most interesting spinel-oxide structures that are used in many fields: physics, biomedical, and environmental fields [17, 18] due to their unique electrical and magnetic properties, electronic, photocatalytic ability, and outstanding conductivity [18, 19]. Their excellent electrical conductivity and electrocatalytic activity are due to the presence of surface redox-active centers (B^{3+}/B^{2+}| and A^{3+}/A^{2+}) for O_2 adsorption and activation that arise from the electron bouncing among various valence states of metals in O-sites [15, 20].

MFe_2O_4's physicochemical properties are significantly dependent on the morphology, dimension, crystallographic orientation, and composition of nanostructures [15]. From another point of view, the ORR efficiency is mainly affected by the mass transfer, so for high performance and ideal ORR catalysts, a model carbon support material is required [1]. This support should display high electrical conductivity, good mechanical properties, chemical stability [12], relative chemical inertness [13], high porosity, and high surface [21]. Conductive carbon supports such as carbon nanotubes, graphene oxide, carbon black, and activated carbon (AC) are highly accepted solutions to enhance the electrocatalytic properties of ORR in MFC applications [11, 22].

Among these carbon materials, AC is preferred because it has good characteristics such as its availability on a large scale from secondary sources [8], its low cost [23], and mesoporous structure (2–50 nm) [24] since mesopores could improve the diffusion of oxygen molecules by limiting the decrease in surface area, increasing the exposed active sites, and facilitating the charge transport to and from the catalytic site [21, 24]. This improves the electrical conductivity and the electrocatalytic activity [13]. Using AC as support for MFe_2O_4 spinel oxides is a promising approach to improve its ORR electrocatalytic properties so it could be used in a

neutral solution [25]. The incorporation of magnetic metal oxide nanoparticles onto the AC surface is widely reported all over the literature [25], for example, $CoFe_2O_4$/AC composites [26], $CuFe_2O_4$/AC adsorbents [27], and $MnFe_2O_4$/AC composites [28].

Besides the above factors, the ORR activity of the metal oxides is strongly dependent on synthesis strategies [15]. The traditional methods for the synthesis of ferrite materials have some drawbacks like non-uniform and large particle size, impurities, and low surface area, which seriously reduce their catalytic activity and prevent further improvement in their performance [15, 29]. To overcome these difficulties, some wet chemical processes like the solvothermal method, co-precipitation technique, sol–gel processing, microemulsion, and auto-combustion are used for the production of MFe_2O_4 powders with excellent properties to meet the requirements of the new applications [15, 19, 29]. Co-precipitation is a facile method that is often used to synthesize multi-metal oxides due to its simplicity, the homogeneity of the obtained material, and the application of low temperatures [18, 30]. Additionally, the synthesis of nanocomposite at a higher pH imparts its higher stability, so, a pH > 10 is selected during the co-precipitation. Also, a low-temperature hydrothermal synthesis is assumed to be beneficial in preventing nanoparticle agglomeration, enhancing the interaction of metallic moieties with the carbon support, and retaining structural integrity to favor mass and charge transport [30].

According to the published literature, only a few studies reported the kinetics carried on MFe_2O_4-based AC catalysts at neutral pH in MFCs. Since then, the kinetics behavior of those catalysts in neutral conditions has remained elusive, and the ORR mechanism under investigation has been complicated and is still not fully understood [4, 31]. Kodali et al. [32] discovered that comparing existing literature on MTMO-based-carbon ORR cathode catalysts in MFCs is quite complicated and becomes even more difficult to determine for the following reasons: (i) the catalysts are frequently prepared using different precursors and fabrication methods, and (ii) the performances are only compared to Pt or AC. Also, (iii) various working conditions lead to more diversity in the output, and (iv) it has not been well-established which transition metal (M = Fe, Co, Mn, Ni, etc.) -based carbon catalysts have superior ORR electrochemical performance in neutral media.

The present study introduces the synthesis of novel MFe_2O_4-based AC composites by a combination of different transition metals (Fe, Cu, Mn, and Ni) via a facile co-precipitation approach. The as-synthesized materials are characterized by physicochemical tools, and their ORR electrochemical performance is studied using cyclic voltammetry (CV) and linear sweep voltammetry (LSV) in neutral media (phosphate buffer solution, pH = 7).

Experimental

Materials and reagents

Carbon Vulcan XC-72R was purchased from Fuel Cell Store (USA), nitric acid, manganese (II) nitrate hydrate, ethanol, urea, and sodium hydroxide pellets were purchased from Honeywell, iron(III) nitrate nonahydrate was purchased from Alpha ChemiKa, nickel(II) nitrate hexahydrate was purchased from Alfa Aesar, copper(II) nitrate trihydrate was purchased from Fisher Scientific, and polyethylene glycol 20,000 was purchased from Merck. All materials and chemicals were used with no further purification.

Preparation of electrocatalysts

The as-received Carbon Vulcan XC-72R was chemically treated as previously described [33]; in brief, 3.0 g of carbon vulcan dispersed in 150 ml of nitric acid was sonicated in an ultrasonic bath for 1 h and then mechanically stirred at 60 °C for 3 h. The treated carbon vulcan was then washed with deionized (DI) water until reaching a neutral pH and dried in a vacuum drier at 90 °C till the treated carbon reached a constant weight. The acid-treated carbon (activated carbon; AC) was used as a support for the metal ferrite: $MnFe_2O_4/AC$, $CuFe_2O_4/AC$, and $NiFe_2O_4/AC$.

Typically, $MnFe_2O_4/AC$ nanocomposite was synthesized according to the following modified methods: [34–36] and as shown in Fig. 1; 3.0 g of AC was dispersed in 250 ml of DI water and sonicated using an ultrasonic probe for 30 min.

Under uniform mixing and constant magnetic stirring, 50 ml of PEG and 20 ml of urea aqueous solution were added to ferric nitrate and manganese nitrate solutions (solution 1). PEG was used as a coating agent to prevent nanoparticles from agglomeration during the precipitation process [37]. Solution 1 was added to the dispersed AC. The total mixture was heated at 80 °C for 4 h under constant mechanical stirring for gel formation and full access of the metals in the solution to the AC surface. The co-precipitation of transition metal oxides was achieved at 12.5 pH by the addition of NaOH aqueous solution. Then, the solution was filtered and washed with distilled water several times till neutral pH was attained, and dried at room temperature for 24 h under a vacuum. The obtained dried powder was sonicated in the remaining 100 ml PEG solution for 30 min, filtered, and washed with DI water several times to obtain the PEG-coated $MnFe_2O_4/AC$ composite nanoparticles. The composite was dried in a vacuum oven drier up to a constant weight. All the above steps were repeated to prepare the other two combinations: $NiFe_2O_4/AC$ and $CuFe_2O_4/AC$. Finally, all the prepared composites were calcined at 550 °C for 5 h.

Physical characterization techniques of catalysts

The crystal structure of the composites was analyzed by X-ray diffraction (XRD) (Pan Analytical Model X'Pert Pro) equipped with a Cu-$K\alpha$ radiation source ($\lambda = 0.1542$ nm). Fourier transform infrared spectroscopy (FTIR) was measured by the Nicolet Is-10 FTIR spectrophotometer adopting
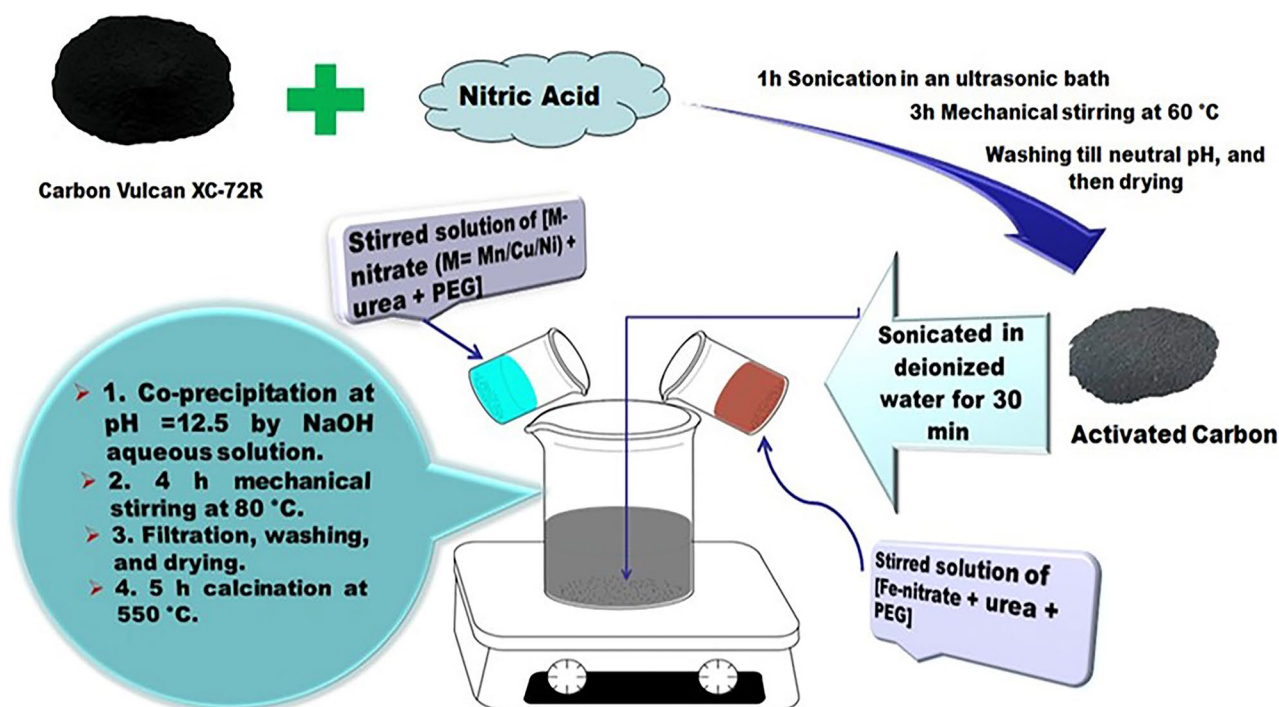

Fig. 1 Schematic diagram of the synthesis procedure

the KBr technique; Thermo Fisher Scientific and Raman spectra were recorded at room temperature by SENTerra Bruker with a 532-nm excitation laser source. The surface morphology for all samples was investigated by field emission-scanning electron microscopy (FE-SEM, ZWESS, FEG (Field Emission Gun)) equipped with an energy dispersive X-ray spectrometer (EDX) operating at resolution (eV) 128.8, Amp time (μs) 3.84, live time (s) 100, Mag:49, and KV:5. The microanalysis was examined using high-resolution transmission electron microscopy (HR-TEM, JEOL JEM-1230). Particle size measurements of the synthesized composites were determined by dynamic light scattering (DLS) measurements using a Zetasizer Nano ZS (Malvern Instruments, UK). The nitrogen adsorption–desorption isotherms were determined by Quantachrome NOVA 3200 automated gas sorption system, USA at -196 °C and after degassing at 120 °C and 10^{-5} mm Hg for 24 h to calculate the Barrett-Joyner-Halenda (BJH) surface area and pore size distributions based on the desorption branches of the isotherms. Electron spin resonance (ESR) was done using a Bruker, Germany through a standard rectangular cavity of ER 4102. Electromagnetic radiation is a coupled electric field (E) and magnetic field (H), and it oscillates at the same frequency (v) within a range of 1–100 GigaHertz (1 Hz = 1 cycle per second). The number of spins (N) is calculated based on the following equation:

$$N = K \frac{H_e \times (\Delta H)^2 \times (\frac{P.H}{wt})}{G_e \times H_m \times \sqrt{P}} \quad (1)$$

where:

N No. of spins, $H_◦$ magnetic resonance, ΔH peak width, G_e gain, H_m modulation amplitude, P power, and K EPR constant = 10^{13} spins

Electrochemical measurements

The electrocatalytic activity of the synthesized catalysts toward ORR was evaluated by CV and LSV. These measurements were carried out at room temperature in a normal three-electrode system using a Voltamaster 6 Potentiostat and a rotating disk electrode (RDE) with a rotation speed control unit. The system consists of platinum (Pt) wire (as a counter electrode), an Ag/AgCl electrode (as a reference electrode), and a glassy carbon electrode (GCE; with a geometrical surface area of 0.196 cm^2) coated with the catalyst thin film as a working electrode.

Before catalyst loading on GCE, it was polished with 0.05 μm alumina powder to obtain a mirror-like surface. Then, it was washed with DI water and acetone. After that, GCE was loaded with a paste of 1 mg catalytic powder mixed with a drop of isopropanol. Then, a drop of 5 wt% Nafion solution (as a binder) was added after isopropanol drying. Finally, the second drop of isopropanol was added

to the paste, and it was let to dry overnight at room temperature. In this study, all the measured potentials were relative to the potential of the Ag/AgCl electrode, and the current densities have been normalized to the electrode geometric area.

Before conducting any electrochemical test, we perform 50 cycles with a scan rate of 50 mV s^{-1} to clean the catalyst surface. Any electrochemical test for oxygen reduction was repeated 10 times until reaching the steady-state performance and taking the last one as a final result. CV and LSV tests were carried out in N$_2$- and O$_2$-saturated 0.1 M (100 mM) phosphate buffer aqueous solution (PBS; as the electrolyte for electrochemical experiments, pH = 7.2) at scan rates of 50 mV s^{-1} and 10 mV s^{-1}, respectively. LSV was conducted at different rpm values (0–1400 rpm) in a voltage range (-1000 to 1000 mV/Ag/AgCl). Before CV and LSV, the electrolyte was bubbled with N$_2$ and O$_2$ for 20 min and half an hour, respectively. The exact ORR kinetic parameters including kinetic current density (J_K) and electron transfer number (n) were analyzed based on the Koutecky-Levich (K-L) equation [6] as follows:

$$\frac{1}{j} = \frac{1}{j_L} + \frac{1}{j_k} = \frac{1}{B\omega^{\frac{1}{2}}} + \frac{1}{j_k} \quad (2)$$

$$B = 0.62 \, n \, F \, C_◦ \, (D_◦)^{\frac{2}{3}} \, v^{\frac{-1}{6}} \quad (3)$$

where j, j_L, and j_K are the measured, limiting diffusion, and kinetic current density (mA cm^{-2}), respectively, and ω represents the electrode rotation speed. B is the slope of the K-L plot, n is the number of electrons transferred per O$_2$ molecule in ORR, and F is Faraday's constant ($F = 96,487$ C mol^{-1}). In 0.1 M PBS, $C_◦$ (1.117×10^{-6} mol mL^{-1}) is the O$_2$ bulk concentration, $D_◦$ (1.9×10^{-5} cm^2 s^{-1}) is the O$_2$ diffusion coefficient, and v (0.01073 cm^2 s^{-1}) is the electrolyte kinetic viscosity [31].

Results and discussion

Electrocatalysts physical characterization

XRD analysis

Figure 2a shows the XRD pattern of activated carbon, with a distinct broad peak at $2\theta \approx 25°$ and a weak peak at $2\theta = 43°$ corresponding to (002) and (100) crystallographic planes, respectively. The recorded peaks were indexed to the hexagonal crystalline activated carbon [21, 38].

Figure 2b shows the XRD patterns of MnFe$_2$O$_4$/AC, CuFe$_2$O$_4$/AC, and NiFe$_2$O$_4$/AC. CuFe$_2$O$_4$/AC exhibited spinel diffraction peaks at 2θ values of 18.39$^°$, 30.06$^°$, 34.69$^°$, 36.15$^°$, 44.11$^°$, and 62.19° which correspond to crystallographic
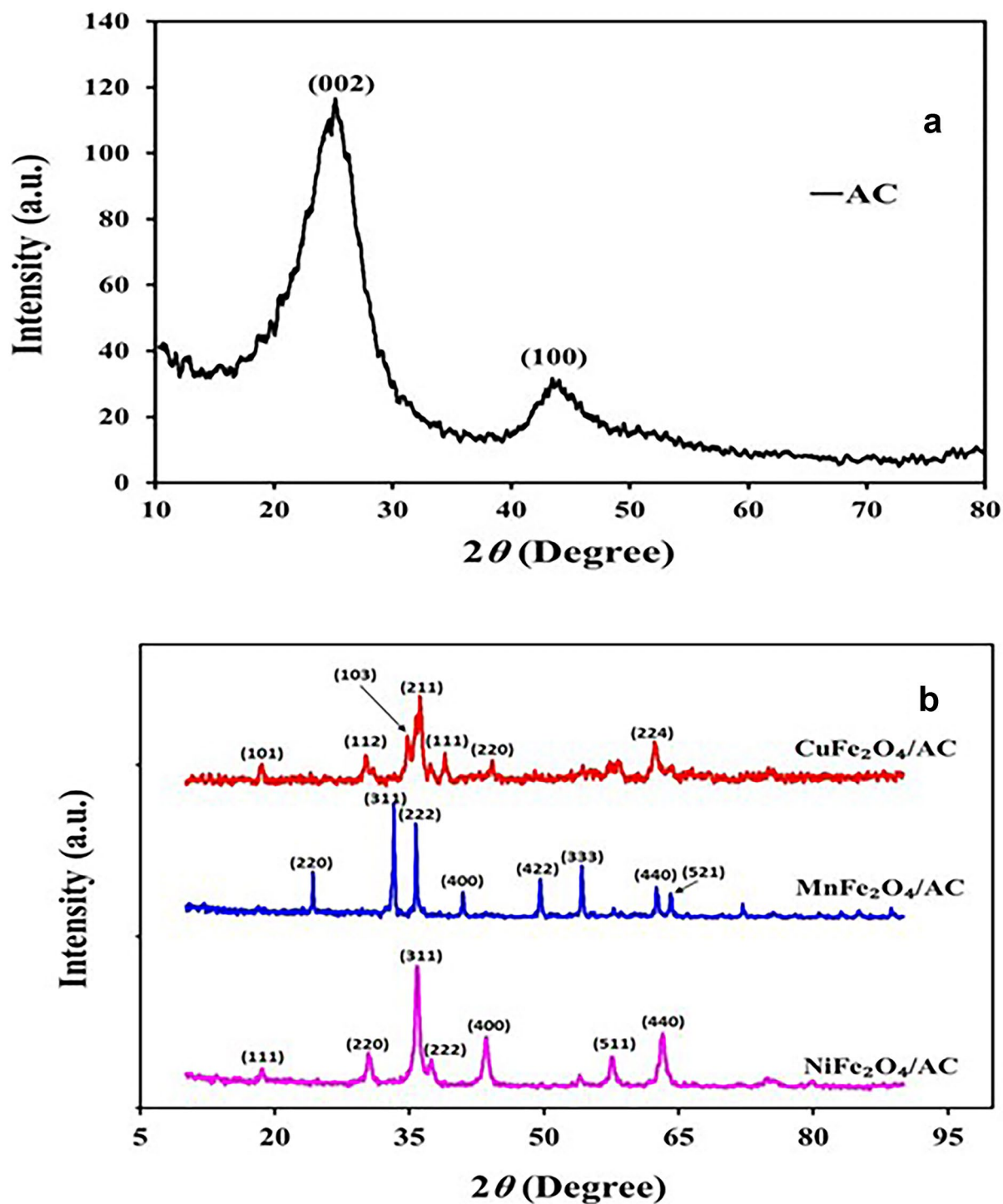
Fig. 2 XRD of (**a**) AC and (**b**) $CuFe_2O_4/AC$, $MnFe_2O_4/AC$, and $NiFe_2O_4/AC$

planes (101), (112), (103), (211), (220), and (224) respectively, in agreement with the literature [27] (ICDD: 04–006-4007). Furthermore, $CuFe_2O_4$/AC spectra showed the presence of a weak peak at $2\theta = 38.91°$ for CuO (111) [39] (ICDD: 04–006-4186). Spinel diffraction peaks were observed in $MnFe_2O_4$/AC spectra at $2\theta = 24.25°$, $33.25°$, $35.65°$, $41.03°$, $49.59°$, $54.15°$, $62.51°$, and $64.21°$ congruent to (220), (311), (222), (400), (422), (333), (440), and (521), which agrees with the literature [40, 41]. The $MnFe_2O_4$/AC main diffraction peak at $2\theta = 33.25°$ is considered a measurable degree of its crystallinity [42], and its sharpness indicates that the $MnFe_2O_4$/AC possesses a higher crystallinity [29]. Finally, $NiFe_2O_4$/AC has diffraction peaks at $2\theta = 18.52°$ (111), $30.38°$ (220), $35.80°$ (311), $37.43°$ (222), $43.48°$ (400), $57.59°$ (511), and $63.11°$ (440) [43] (ICDD: 04–006-6580). Upon the deposition of different TMOs on the AC surface, the intensity of carbon peaks decreased due to the decrease in graphitization degree, and this proves the combination of metal oxides with AC [5].

Raman spectroscopy

Figure 3 shows the Raman spectrum of $NiFe_2O_4$/AC and AC. The Raman spectra of AC exhibited two obvious peaks around 1332 cm^{-1} (D band) and 1609 cm^{-1} (G band) of carbon-based materials [44]. Generally, the D peak is concerned with a sequence of lattice defects and carbon atoms' disorder degree, including bond angle and bond length disorder, as well as hybridization. The G peak is evolved from the in-plane stretching vibration of sp^2 hybridized carbon atoms, and it reveals the carbon graphitization degree [45]. The peak intensity ratio of ID/IG could be used to evaluate the degree of defects and disordered structures for each material [46]. The ID/IG ratio of the AC sample is approximately equal to 1.06 implying the good defect degree of this sample. In general, the appropriate defect structure and higher disorder degree in carbon-based catalysts would benefit in increasing the affinity of oxygen adsorption by supplying
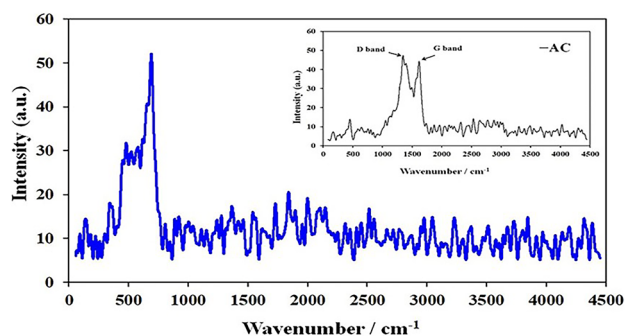
more active sites, thus enhancing the ORR catalytic activity [22, 47]. The deposition of transition metals (Fe, Cu, Mn, and Ni) on the AC surface affected the D and G bands, and these Raman bands disappeared after the deposition, thereby changing the ID/IG value. This change is ascribed to the change in geometry, purity, crystallinity, structure, and surface composition of the AC. However, Fig. 3 showed that $NiFe_2O_4$/AC exhibited peaks around 486 and 691 cm^{-1} that were pointed to NiO, while no peaks were detected for $CuFe_2O_4$/AC and $MnFe_2O_4$/AC, since these composites are Raman silent [48]. These results proved the deposition of Fe, Ni, Cu, and Mn on the AC surface.

FT-IR spectroscopy

The structures of AC, $CuFe_2O_4$/AC, $MnFe_2O_4$/AC, and $NiFe_2O_4$/AC were examined by FT-IR spectroscopic analysis as shown in Fig. 4. The FT-IR spectra of the prepared materials showed strong bands in the lower mid-infrared 400–700 cm^{-1} range that originate from the stretching vibrations of the metal–oxygen bond (M–O; M = Mn, Ni, Cu, and Fe) [13]. The strong peaks observed at 578 and 619 cm^{-1} were attributed to (Mn–O) and (Ni–O) stretching vibration bands of $MnFe_2O_4$/AC and $NiFe_2O_4$/AC, respectively [42, 48]. In the case of $CuFe_2O_4$/AC, the peak at 430 cm^{-1} was assigned to Fe–O, while the peak at 603 cm^{-1} was confirmed to Cu–O bond [49, 50]. The peaks around 1140 cm^{-1} were devoted to (C–N) stretching vibrations for $MnFe_2O_4$/AC and $NiFe_2O_4$/AC, whereas the peak at 1543 cm^{-1} was assigned to (N–H) bending of amide II for $CuFe_2O_4$/AC, $MnFe_2O_4$/AC, and $NiFe_2O_4$/AC [51, 52]. All the fabricated materials show a peak around 1650 cm^{-1} assigned to (C=O stretching) [48, 50]. All the catalysts (AC, $CuFe_2O_4$/AC, $MnFe_2O_4$/AC, and $NiFe_2O_4$/AC) show a strong and broad peak around 3450 cm^{-1} due to the presence of (OH-free asymmetric stretching), which is attributed to the physisorbed water

Fig. 3 Raman spectra of $NiFe_2O_4$/AC and AC
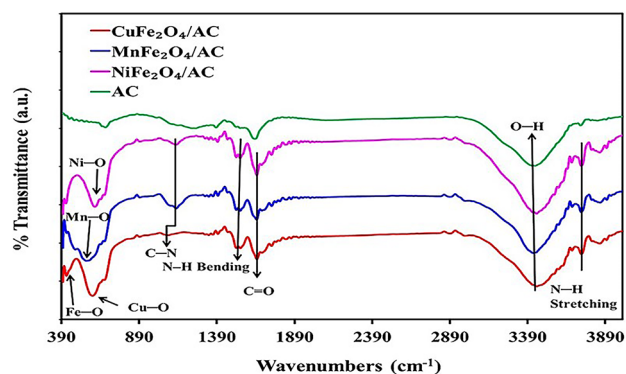
Fig. 4 FT-IR of $CuFe_2O_4$/AC, $MnFe_2O_4$/AC, $NiFe_2O_4$/AC, and AC

molecules that were absorbed from the surrounding atmosphere [13, 21, 48]. The absorption peak around 3650 cm^{-1} (one peak) is assigned to (N–H) stretching frequency of amide II.

Surface analysis

The surface properties and the pore structure of the prepared composites (MnFe$_2$O$_4$/AC, CuFe$_2$O$_4$/AC, and NiFe$_2$O$_4$/AC) were studied by N$_2$ adsorption–desorption isotherms. It is commonly regarded that carbon materials with a multi-level porous structure provide a large number of catalytic active sites with fine dispersion and suitable channels to facilitate reactant diffusion and electron transfer [53]. Figure 5a showed that the catalysts exhibited classical type IV isotherms and a well-defined hysteresis loop close to high relative pressure in the $P/P_\circ$ range (0.7–1) for all samples, which is characteristic for mesoporous materials. This is greatly important to ORR since mesopore is mainly required to enable mass transport of sufficient oxygen in ORR [10, 54]. Furthermore, according to the desorption branch, the BJH surface area and total pore volume of MnFe$_2$O$_4$/AC, CuFe$_2$O$_4$/AC, and NiFe$_2$O$_4$/AC catalysts have partially decreased than that of AC after deposition, which could be due to pore-filling and pore-blocking of channels during the precipitation process [1], as confirmed by the disappearance of AC micropores in the prepared composites.

As listed in Table 1, MnFe$_2$O$_4$/AC had a low BJH surface area of 53.236 m^2 g^{-1} with a total pore volume of 0.09 cm^3 g^{-1}, all of which originated from mesopores compared to that of AC that possessed a high BJH surface area of 180.149 m^2 g^{-1} and total pore volume of 0.44 cm^3 g^{-1}. The decrease in BJH area resulted from a decrement in mesopores that was likely owed to the occupancy of partial mesopores for AC by the deposition of Mn and Fe nanoparticles [13]. The BJH surface area and total pore volume of mesopores were slightly increased in CuFe$_2$O$_4$/AC compared to MnFe$_2$O$_4$/AC, to be 56.481 m^2 g^{-1} and 0.1 cm^3 g^{-1}, respectively. On the other hand, the BJH surface area and total pore volume of mesopores in NiFe$_2$O$_4$/AC were

Table 1 Structural and textural parameters for MnFe$_2$O$_4$/AC, CuFe$_2$O$_4$/AC, and NiFe$_2$O$_4$/AC composites

Catalyst	S_{BJH}/m^2 g^{-1}	V_p/cm^3 g^{-1}	d$V(r)$/nm
AC	180.15	0.44	8.17
MnFe$_2$O$_4$/AC	53.24	0.09	10.48
CuFe$_2$O$_4$/AC	56.48	0.10	11.83
NiFe$_2$O$_4$/AC	76.26	0.27	50.50

S_{BJH} surface area estimated by BJH equation, V_p total pore volume (PV) calculated at $P/P_\circ = 0.99$, d$V(r)$ pore radius

remarkably increased to be 76.259 m^2 g^{-1} and 0.27 cm^3 g^{-1}, respectively.

Pore size distribution curves are shown in Fig. 5b, pointing out that all the samples have mesopore sizes in the range of 10–50 nm. This indicates that mesopores contributed the majority of the volume, which was thought to be beneficial for ORR and the transport of electrolyte ions (proton) into the interior catalyst layers, while their pore sizes are 10.476, 11.831, and 50.501 nm for MnFe$_2$O$_4$/AC, CuFe$_2$O$_4$/AC, and NiFe$_2$O$_4$/AC, respectively. In particular, the mesoporous structure is profitable for the rapid transmission of O$_2$, fuel, and electrolytes, which can accelerate the redox reaction rate and improve electrochemical performance [10]. The electrochemical performances are highly linked to the catalysts' surface-active sites and mobility into the electrolyte [46].

FE-SEM and EDX microscopy

Figure 6 shows the FE-SEM images, mapping, and EDX analysis obtained for MnFe$_2$O$_4$/AC, CuFe$_2$O$_4$/AC, and NiFe$_2$O$_4$/AC composites. The morphology of all the prepared samples shows to some extent a spherical-like nanoparticle aggregate and uniformly grown on the AC surface [13]. Generally, using AC as a support improves the dispersion of the transition metal oxides and reduces their agglomeration [50]. As shown in Fig. 6, CuFe$_2$O$_4$/AC shows spherical nanoparticles sintered together to form a connected structure with a smaller primary size 44.7–71.6 nm. The micrographs of NiFe$_2$O$_4$/AC

Fig. 5 (**a**) N$_2$ adsorption–desorption isotherms and (**b**) pore size distribution for MnFe$_2$O$_4$/AC, CuFe$_2$O$_4$/AC, and NiFe$_2$O$_4$/AC
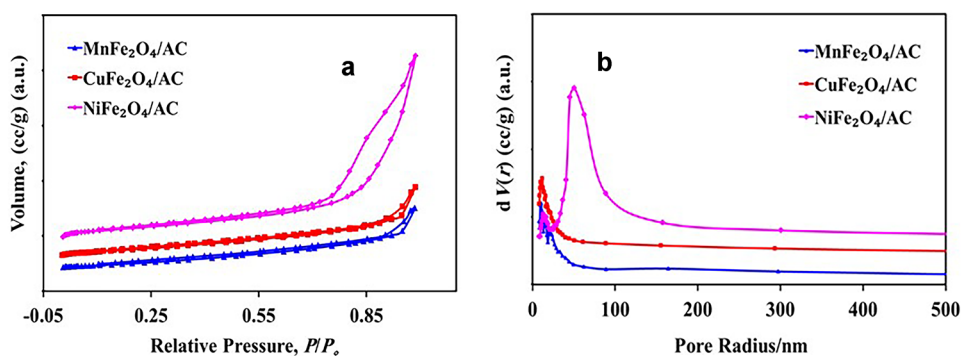
Fig. 6 SEM, Mapping, and EDX Images for CuFe2O4/AC, NiFe2O4/AC, and MnFe2O4/AC
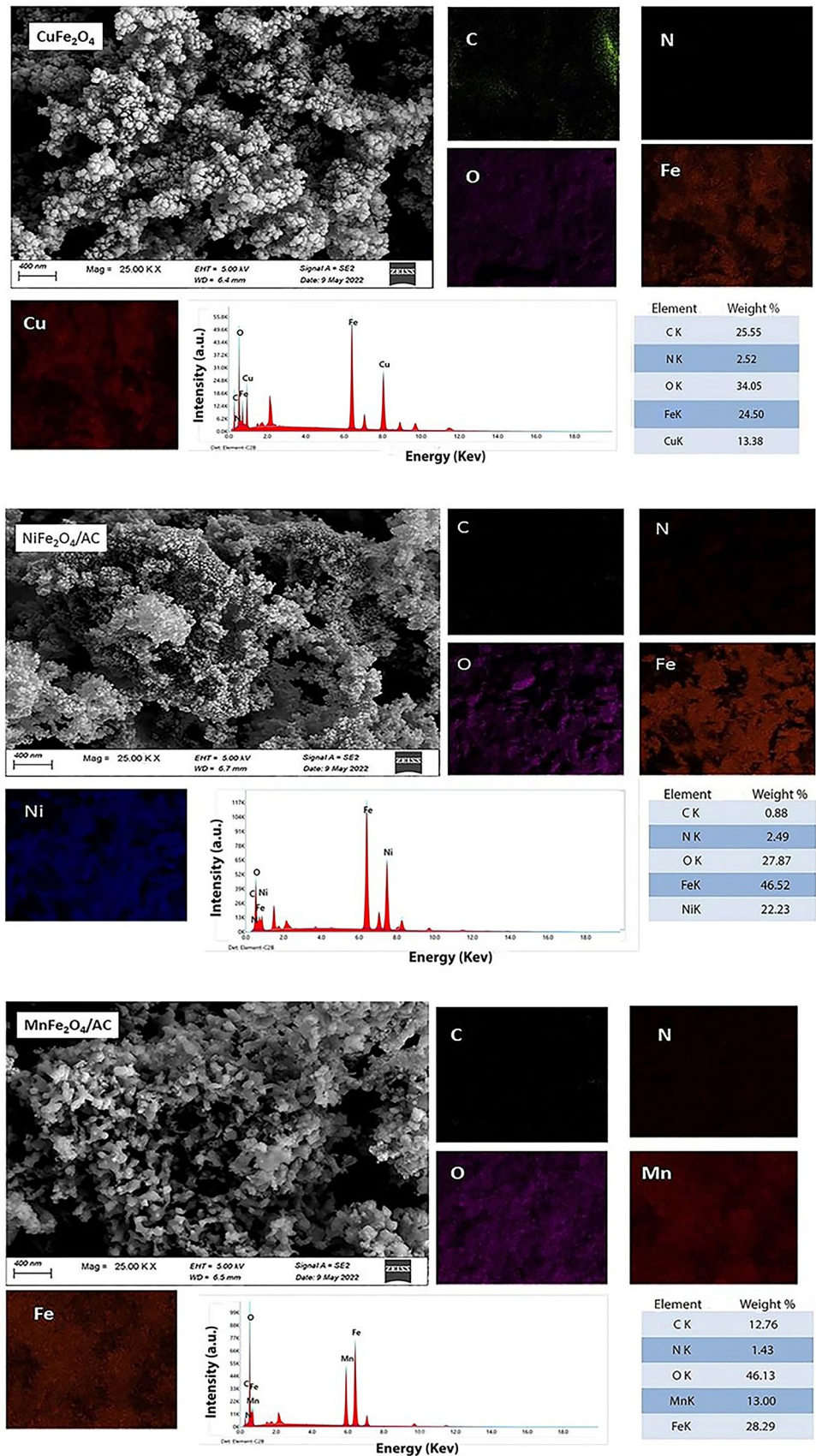
show clusters of fine particles sticking jointly. The sample surface contains number of fine pores or voids (defects) that could be attributed to the large quantity of gases released during the calcination process. The grain size estimated from the micrograph is in the range of 19.97–43.98 nm. $MnFe_2O_4$/AC reveals semi-quasispherical particles with unqualified sharp crystals in a cluster shape, homogeneously distributed in the AC frame. The grain size ranged from 35.78 to 107.6 nm. The EDX spectrum analysis confirms the characteristic peaks of the Cu, Fe, Mn, Ni, C, N, and O, while no other peaks of foreign elements were observed. The involved table in Figure 5 depicts the wt.% of Cu, Fe, Mn, Ni, C, N, and O elements, and it proves the presence of these elements in the prepared composites. The chemical analysis showed that the Wt% Fe/wt% Cu=1.83 and the at% of Fe/at%Cu= 2.08 while the Wt% of Fe/wt% of Ni=2.09 and the at% of Fe/Ni=2.1 and Wt% of Fe/ Mn= 2.17 and the at% of Fe/Ni=2.13. This proves the formation of spinels. The consistent elemental mappings in selected areas additionally reveal a homogeneous distribution of O, Fe, C, N, Mn, Cu, and Ni. Remarkably, carbon had the lowest percentage of all the prepared composites, revealing that the metal-oxide layers covered most of the catalysts' surface [48]. These results are consistent with the FE-SEM findings.

HR-TEM and DLS analysis

HR-TEM of carbon vulcan (Fig. 7a) shows aggregated particles with spherical shape and irregular size. The reduction in size and ordered uniform structure (Fig. 7b) is noticed and attributed to the shrinkage and dispersion of particles during the acidic treatment of carbon vulcan. TEM images of all composites show low agglomeration, high dispersion, and homogeneous distribution of the composite nanoparticles on the AC surface [10, 50]. $CuFe_2O_4$/AC (Fig. 7c) displays a uniform and wide distribution cuboid structure, and the DLS analysis shows that the average particle size is 712 nm. Figure 7d of $NiFe_2O_4$ displayed a semi-spherical particles with a random range of particle size (295–995 nm) as confirmed in the histogram of DLS analysis. HR-TEM image of $MnFe_2O_4$ (Fig. 7e) reveals the shell formation of the hollow nanoparticles, which are made up of some nanocrystals. There are fundamentals for the formation of a hollow structure as follow [55]: (1) a deep permeation of metal ions within the carbon nanoparticles, and (2) the two rates of the precursor shell formation and that of carbon nanosphere decomposition must match with each other. When the heating temperature is low, the breakdown rate of the carbon species is slow, allowing the metal atoms to assemble within the carbon templates and interconnect to form shell layers. The diameter distribution from the DLS curve shows that $MnFe_2O_4$ has a wide range (220–1106 nm) of particle size.

ESR spectroscopy

Electron spin resonance (ESR) measurements were carried out to verify the presence of oxygen vacancies and demonstrate the assimilation of the oxygen defects, qualitatively, in $MnFe_2O_4$/AC, $CuFe_2O_4$/AC, and $NiFe_2O_4$/AC. Figure 8 points out that all the samples display a single ESR signal at a g-value of 2.29 ($g//$) and 2.7 ($g\perp$) for $MnFe_2O_4$/AC. A $CuFe_2O_4$/AC sample has a $g//$ of 2.49 and a $g\perp$ of 2.91, whereas $NiFe_2O_4$/AC has a $g//$ of 2.42 and a $g\perp$ of 2.93, which is related to unpaired electrons trapped in oxygen vacancies (O_V) [56].

The magnetic properties can be illustrated by peak-to-peak line width (ΔH_{pp}), resonant magnetic field (H_r), and g-factor [57]. Table 2 shows that ΔH_{pp} values increase from 671.9 to 972.3 and 1019.8 Oe for $CuFe_2O_4$/AC, $NiFe_2O_4$/ AC, and $MnFe_2O_4$/AC, respectively. Strong dipole interactions resulted in a large broad peak-to-peak line width (ΔH_{PP}) and higher crystallite size. Our results show that the broad signal narrows down with $MnFe_2O_4$/AC and it gives the highest H_r (Oe), while small ΔH_{PP} gives rise to strong super-exchange interactions as in $NiFe_2O_4$/AC. However, the large ΔH_{PP} indicates the large ferrimagnetic particles [58]. ΔH_{PP} was found to decrease with the decrease in crystallite size of the particle due to strong super-exchange interactions. The intensity of the ESR peak is much higher for $NiFe_2O_4$/AC compared with $MnFe_2O_4$/AC or $CuFe_2O_4$/AC. This indicates that $NiFe_2O_4$/AC is opulent in oxygen defects.

It has been recognized that the decrease in the metal oxidation number happens when the crystal consumes an oxygen atom in vacancy formation. Also, theoretically, it was noticed that the reduction in particle size increases the metal stability in its several applications [59].

The g-factor values increase from 2.12 to 2.16 with the increase in the particle size and calcination temperature, hence increasing the microscopic magnetic interactions. In ferrites, the difference between ΔH_{pp} and g-factor values can explain the super-exchange and dipole–dipole interactions [60]. Table 2 illustrates that the value of the resonant magnetic field reduces from 2989 to 2976 Oe due to the incorporated metal.

Electrochemical performance of the electrocatalysts toward ORR

The ORR activity of $CuFe_2O_4$/AC, $MnFe_2O_4$/AC, and $NiFe_2O_4$/ AC composites was investigated using RDE measurements (CV and LSV) in N_2- and O_2-saturated 100 mM PBS neutral solution at scan rates of 50 mV s^{-1} and 10 mV s^{-1}, respectively. Figure 9 shows the CVs of $CuFe_2O_4$/AC, $MnFe_2O_4$/AC, and $NiFe_2O_4$/AC composites, which reveals that no redox peaks were observed for the samples in both the absence (black line) and presence (red line) of oxygen. In the presence of oxygen,
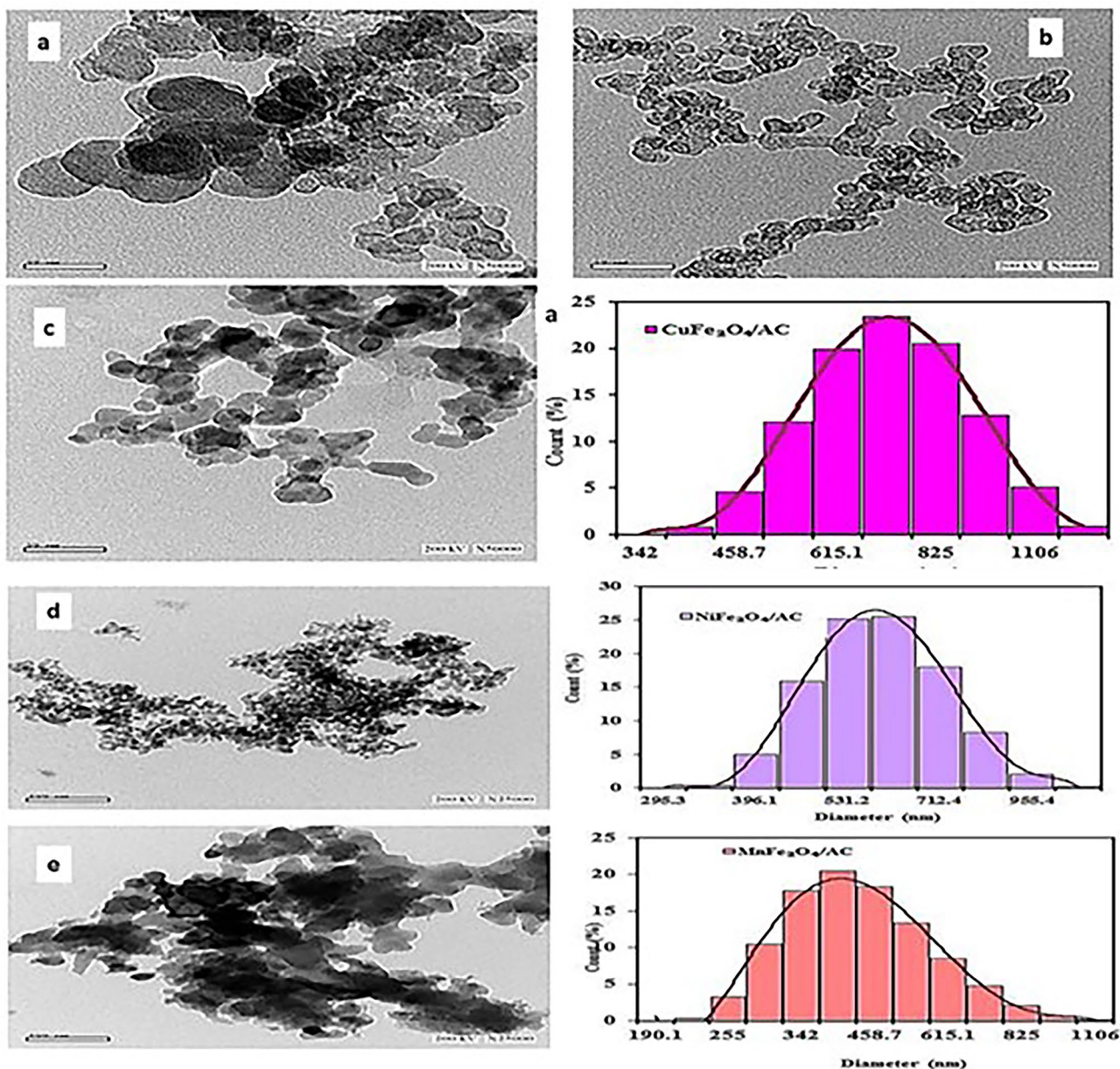
Fig. 7 HR-TEM images for (**a**) carbon vulcan, (**b**) AC, (**c**) $CuFe_2O_4$/AC, (**d**) $NiFe_2O_4$/AC, and (**e**) $MnFe_2O_4$/AC

all of the composites demonstrated capacitive behavior and efficient catalytic activity toward ORR [14]. $MnFe_2O_4$/AC has a higher ORR activity than $NiFe_2O_4$/AC and $CuFe_2O_4$/AC because at potential -24 mV vs. Ag/AgCl, $MnFe_2O_4$/AC exhibits a larger current density (-138.2 μA cm^{-2}) response than $NiFe_2O_4$/AC (-104.75 μA cm^{-2}) and $CuFe_2O_4$/AC (-83.09 μA cm^{-2}).

For more studying the electrochemical properties of the prepared composites, the background subtraction of cyclic voltammetry (BS-CV) technique is applied. The concept of background current subtraction denotes to subtraction of current density in the presence of O_2 to the current density without O_2 to exclude the reaction of the background solution [61]. After using BS-CV technique (Fig. 9), no redox peaks were observed for the three samples. The BS-CV (green line) reveals that the electrocatalysts still keep on their capacitive behavior, and this confirms its electrocatalytic activity.
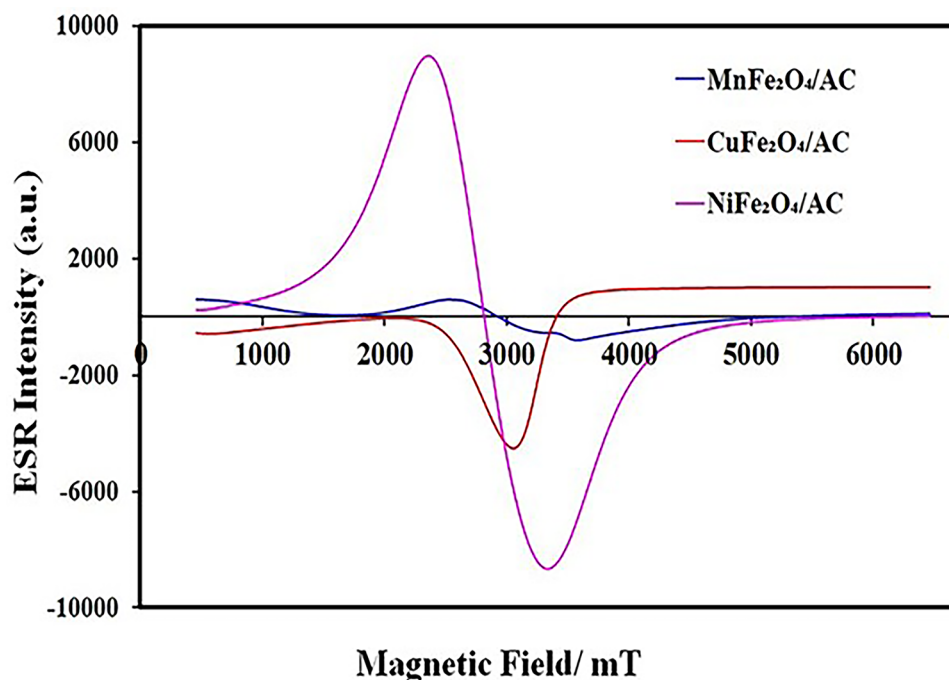
To further investigate the ORR performance of CuFe$_2$O$_4$/AC, MnFe$_2$O$_4$/AC, and NiFe$_2$O$_4$/AC composites, LSV tests were performed in an O$_2$-saturated 100 mM PBS neutral medium at different rpm by employing a voltage that varies linearly across the working electrode and recording the corresponding current change. Figure 10a shows that MnFe$_2$O$_4$/AC had onset potential (E_{onset}) (-0.223 V vs. Ag/AgCl) and kinetic current density (j_K) (-5 mA cm^{-2}) higher than CuFe$_2$O$_4$/AC (-0.280 V vs. Ag/AgCl, -3.05 mA cm^{-2}), and NiFe$_2$O$_4$/AC (-0.270 V vs. Ag/AgCl, -2.67 mA cm^{-2}). This implies that MnFe$_2$O$_4$/AC has enhanced catalytical activity and is kinetically more facile for O$_2$ reduction, so it is the highest ORR active electrocatalyst among the prepared composites in this work.

Additionally, the kinetic performance of the prepared composites was further evaluated by Tafel plots which were calculated from the LSV curve at 800 rpm (Fig. 10b). The Tafel curve is one of the main indicators for ORR catalytic activity. The electrocatalyst Tafel slopes are in the order of MnFe$_2$O$_4$/AC (-330 mV dec^{-1}) < NiFe$_2$O$_4$/AC (-414 mV dec^{-1}) < CuFe$_2$O$_4$/AC (-577 mV dec^{-1}), which agrees with the ORR results. In addition, the Tafel slope

Table 2 ESR data for MnFe$_2$O$_4$/AC, CuFe$_2$O$_4$/AC, and NiFe$_2$O$_4$/AC composites

Sample	ΔH_{pp} (Oe)	H_r (Oe)	N	P.H
MnFe$_2$O$_4$/AC	1019.8	2894.4	4E+23	1389
CuFe$_2$O$_4$/AC	671.9	—	0	4270
NiFe$_2$O$_4$/AC	972.3	2777.1	3E+24	17628

ΔH_{pp} (Oe) line width, N number of spin resonance, $P.H.$ peak height
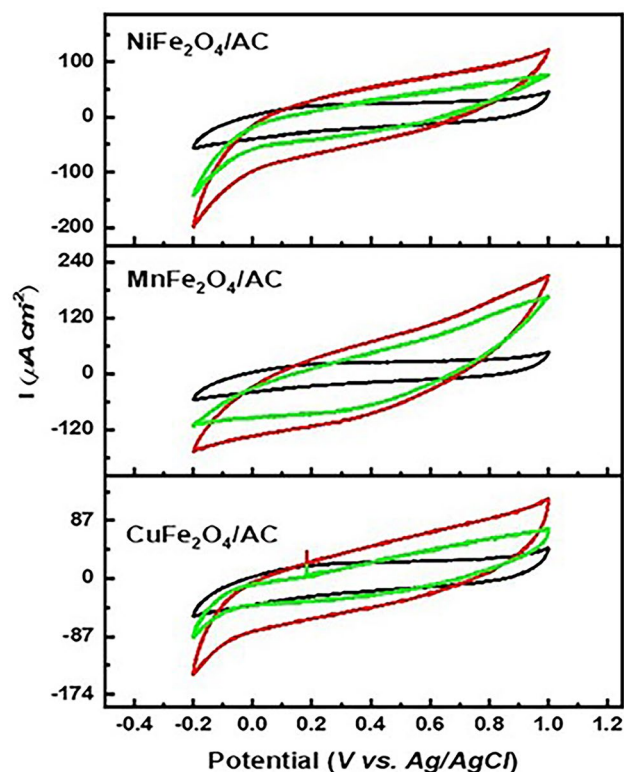
Fig. 9 CV curves in N$_2$-saturated (black line), O$_2$-saturated (red line), and background current subtract (green line) of NiFe$_2$O$_4$/AC, MnFe$_2$O$_4$/AC, and CuFe$_2$O$_4$/AC composites at 50 mV s^{-1}
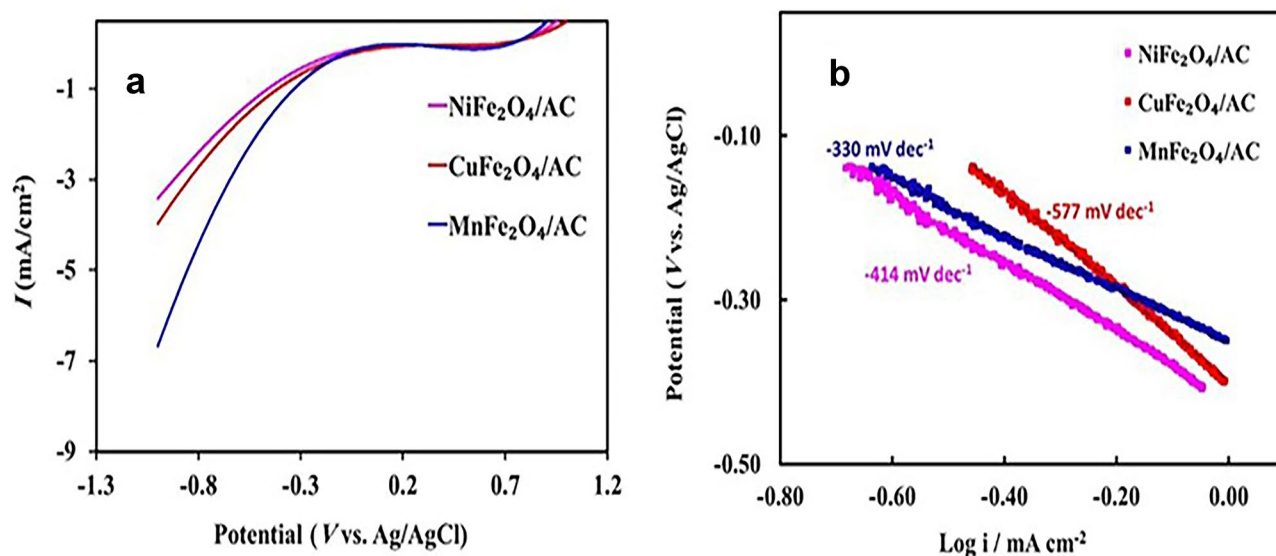
Fig. 10 (**a**) LSV curves comparison of NiFe$_2$O$_4$/AC, CuFe$_2$O$_4$/AC, and MnFe$_2$O$_4$/AC composites at 800 rpm and 10 mV s^{-1} scan rate, and the corresponding (**b**) Tafel fitting lines

is closely related to electron transfer rate, and the fact that the MnFe$_2$O$_4$/AC composite presents the lowest Tafel slope suggests that it can easily adsorb oxygen molecules onto its surface and activate it. Also, this means a quicker electron transfer rate, thereby exhibiting the best and fastest ORR kinetics and performance under neutral conditions [21, 53, 62].

Figure 11a shows that the kinetic and diffusion current density increase with the rotation speed, implying the decrease of diffusion resistance among the catalyst surface and saturated oxygen molecules [46]. Furthermore, the ORR pathway at the MnFe$_2$O$_4$/AC surface was kinetically and quantitatively studied by using the LSV plots collected from RDE experiments performed at different rotation speeds, and the slope of the curve was obtained at applied potentials between −0.5 and −0.7 V vs. Ag/AgCl to calculate the number of electron transfer from the K-L equation.

The fitted lines of K-L plots (Fig. 11b) show good linearity at different potentials, and this indicates first-order ORR reaction kinetics toward the concentration

of dissolved oxygen in neutral electrolytes [46, 53]. The average electron transfer number was 4.3 demonstrating that ORR catalyzed by MnFe$_2$O$_4$/AC mainly proceeds via a 4-electron mechanism. Among the prepared materials, MnFe$_2$O$_4$/AC showed the highest ORR catalytic activity owing to a good combination of crystal structure and morphology. This improved ORR activity of MnFe$_2$O$_4$/AC can be ascribed to the strong interaction between Fe, Mn, and AC [63]. Besides, the transition valence state of Mn plays an essential role in encouraging the adsorption and reduction of oxygen [12, 64].

Compared with Pt/C electrocatalyst, MnFe$_2$O$_4$/AC displayed current density equal to that of Pt/C (−5.1 mA cm^{-2}) [65]. Also as shown in Table 3, MnFe$_2$O$_4$/AC showed a higher current density than electrocatalysts in the literature. The high electrocatalytic performance of MnFe$_2$O$_4$/AC may be attributed to both the defective structure and mesoporosity of AC and the redox activity of metal centers (Fe and Mn) [30]. Aside from the high dispersion of Fe and Mn nanoparticles [24], and

Fig. 11 (**a**) LSV curves of MnFe$_2$O$_4$/AC composite at different rpm and 10 mV s^{-1} scan rate, and the corresponding (**b**) K-L plots at different potentials
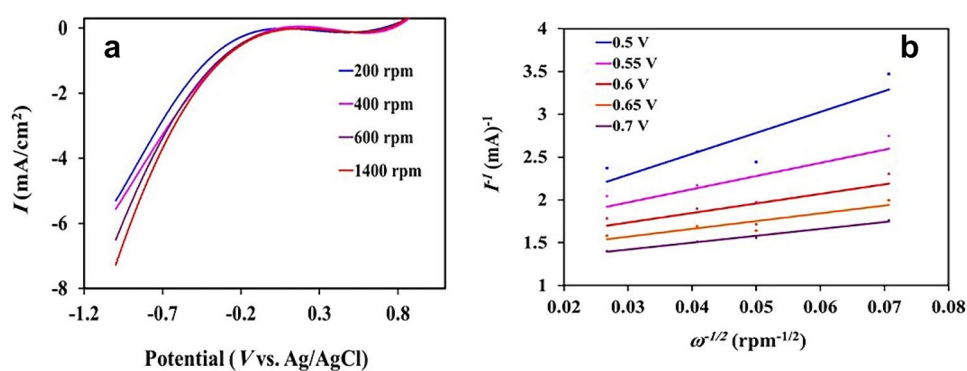
Table 3 ORR performance comparison of electrocatalysts reported in literature

Electrocatalyst	Preparation method	Electrolyte	Current density (mA cm^{-2})	Ref
MnFe$_2$O$_4$/AC	Co-precipitation	PBS	5	This study
MnO$_2$–CuO/AC	Co-precipitation	PBS	4.2	[65]
Fe–N–C	Reflux and pyrolysis	PBS	4	[3]
MNG	Solvothermal	KOH	3.7	[64]
CK	Carbonization	KOH	3	[46]
NiMn$_2$O$_4$	Co-precipitation	PBS	2.47	[66]
Ni–MnO$_x$/monarch	Chemical deposition	Na$_2$SO$_4$	2.8	[67]

the predominant presence of manganese in a + 2 oxidation state, Mn(II) entities are highly accepted as efficient centers for oxygen adsorption and electron transfer via the Mn(II) to Mn(III) transformation [30, 64]. These factors helped in the contact between the active sites and electrolyte solution, hence enhancing the ORR process [12].

Conclusion

MFe$_2$O$_4$/AC composites were successfully prepared and characterized through different routes. The high dispersion of the ferrites on the surface of the carbon is considered to be responsible for the high electrochemical activity. Additionally, our results collected from LSV carried at 800 rpm revealed that MnFe$_2$O$_4$/AC had higher E_{onset} (−0.223 V vs. Ag/AgCl), kinetic current density (j_K) (−5 mA cm^{-2}), and lower Tafel slope (330 mV dec^{-1}) than NiFe$_2$O$_4$/AC (−0.270 V vs. Ag/AgCl, −2.67 mA cm^{-2}, and 414 mV dec^{-1}), and CuFe$_2$O$_4$/AC (−0.280 V vs. Ag/AgCl, −3.05 mA cm^{-2}, and 577 mV dec^{-1}), respectively. Meanwhile, the K-L plot calculations for ORR catalyzed by MnFe$_2$O$_4$/AC in neutral phosphate buffer solution (pH = 7) and at different rpm confirmed that it is a 4e$^-$ pathway mechanism. MnFe$_2$O$_4$ displayed the highest ORR performance, and this can be pointed to (i) mesoporosity that provides more accessibility to active sites, (ii) highly dispersed Mn and Fe species that work as the main active sites, and (iii) the large ferrimagnetic particles. Thus, MnFe$_2$O$_4$/AC is suggested to be a model alternative for the commercial Pt/C catalyst. Finally, this research work has contributed to a simple, efficient, and low-cost synthesis technique for the development of naturally abundant and efficient ORR composite electrocatalysts with improved electrocatalytic performance. MnFe$_2$O$_4$/AC is considered a low-cost Pt-alternative ORR cathode catalyst for MFC applications at pH = 7. We suggest taking into consideration our research results, since it sheds light on the design and synthesis of spinel-structure ferrite oxides and expands their applications in energy conversion technologies, including fuel cells, particularly, MFCs operated in neutral conditions at pH = 7.

Declarations

Conflict of interest The authors declare no competing interests.

References

1. Chen X, Li Z, Qin R et al (2020) Shale-oil-based nitrogen-doped porous carbon as efficient metal-free electrocatalyst for oxygen reduction reaction. Catal Commun 146:1–5. https://doi.org/10.1016/j.catcom.2020.106131
2. Santoro C, Arbizzani C, Erable B, Ieropoulos I (2017) Microbial fuel cells: from fundamentals to applications. A review J Power Sources 356:225–244. https://doi.org/10.1016/j.jpowsour.2017.03.109
3. Ketpang K, Boonkitkoson A, Pitipuech N et al (2020) Highly active and durable transition metal-coordinated nitrogen doped carbon electrocatalyst for oxygen reduction reaction in neutral media. E3S Web Conf 141:0–4. https://doi.org/10.1051/e3sconf/202014101005
4. Merino-Jimenez I, Santoro C, Rojas-Carbonell S et al (2016) Carbon-based air-breathing cathodes for microbial fuel cells. Catalysts 6:1–13. https://doi.org/10.3390/catal6090127
5. Yao Z, Ma J, Hoang TKA et al (2020) High performance biomass-derived catalysts for the oxygen reduction reaction with excellent methanol tolerance. Int J Hydrogen Energy 45:27026–27035. https://doi.org/10.1016/j.ijhydene.2020.07.023
6. Zhang P, Wang R, Xiao T et al (2020) The high-performance bifunctional catalyst Pd/Ti3C2Tx–carbon nanotube for oxygen reduction reaction and hydrogen evolution reaction in alkaline medium. Energy Technol 8:1–7. https://doi.org/10.1002/ente.202000306
7. Zhou R, Zheng Y, Hulicova-Jurcakova D, Qiao SZ (2013) Enhanced electrochemical catalytic activity by copper oxide

grown on nitrogen-doped reduced graphene oxide. J Mater Chem A 1:13179–13185. https://doi.org/10.1039/c3ta13299d

8. Oliveira ACD, M, D'Epifanio A, Ohnuki H, Mecheri B (2020) Platinum group metal-free catalysts for oxygen reduction reaction: applications in microbial fuel cells. Catalysts 10:1–22. https://doi.org/10.3390/catal10050475

9. Wang Y, Ma X, Lu L et al (2013) Carbon supported MnOx-Co3O4 as cathode catalyst for oxygen reduction reaction in alkaline media. Int J Hydrogen Energy 38:13611–13616. https://doi.org/10.1016/j.ijhydene.2013.08.048

10. Fang Y, Wang Y, Wang F et al (2018) Fe-Mn bimetallic oxides-catalyzed oxygen reduction reaction in alkaline direct methanol fuel cells. RSC Adv 8:8678–8687. https://doi.org/10.1039/c7ra12610g

11. Goswami C, Hazarika KK, Bharali P (2018) Transition metal oxide nanocatalysts for oxygen reduction reaction. Mater Sci Energy Technol 1:117–128. https://doi.org/10.1016/j.mset.2018.06.005

12. Zhang Y, Wang Y, Huang J et al (2020) Mn3O4 nanosheets coated on carbon nanotubes as efficient electrocatalysts for oxygen reduction reaction. Int J Hydrogen Energy 45:6529–6537. https://doi.org/10.1016/j.ijhydene.2019.12.216

13. Hazarika KK, Goswami C, Saikia H et al (2018) Cubic Mn2O3 nanoparticles on carbon as bifunctional electrocatalyst for oxygen reduction and oxygen evolution reactions. Mol Catal 451:153–160. https://doi.org/10.1016/j.mcat.2017.12.012

14. Ma TY, Zheng Y, Dai S et al (2014) Mesoporous MnCo2O4 with abundant oxygen vacancy defects as high-performance oxygen reduction catalysts. J Mater Chem A 2:8676–8682. https://doi.org/10.1039/c4ta01672f

15. Si C, Zhang Y, Zhang C et al (2017) Mesoporous nanostructured spinel-type MFe2O4 (M = Co, Mn, Ni) oxides as efficient bi-functional electrocatalysts towards oxygen reduction and oxygen evolution. Electrochim Acta 245:829–838. https://doi.org/10.1016/j.electacta.2017.06.029

16. Yuan C, Bin WuH, Xie Y, Lou XW (2014) Mixed transition-metal oxides: design, synthesis, and energy-related applications. Angew Chemie - Int Ed 53:1488–1504. https://doi.org/10.1002/anie.201303971

17. Kulkarni S, Thombare B, Patil S (2017) MnFe2O4: Synthesis, morphology and electrochemical properties. AIP Conf Proc 1837:3–6. https://doi.org/10.1063/1.4982128

18. Riyanti F, Hariani PL, Purwaningrum W et al (2018) The synthesis of MnFe2O4-activated carbon composite for removal of methyl red from aqueous solution. Molekul 13:123. https://doi.org/10.20884/1.jm.2018.13.2.435

19. Amulya MAS, Nagaswarupa HP, Kumar MRA et al (2021) Sonochemical synthesis of MnFe2O4 nanoparticles and their electrochemical and photocatalytic properties. J Phys Chem Solids 148:109661. https://doi.org/10.1016/j.jpcs.2020.109661

20. Naik KM, Sampath S (2018) Two-step oxygen reduction on spinel NiFe2O4 catalyst: rechargeable, aqueous solution- and gel-based, Zn-air batteries. Electrochim Acta 292:268–275. https://doi.org/10.1016/j.electacta.2018.08.138

21. Mathumba P, Fernandes DM, Matos R et al (2020) Metal oxide (Co3O4 and Mn3O4) impregnation into S, N-doped graphene for oxygen reduction reaction (ORR). Materials (Basel) 13:1562. https://doi.org/10.3390/ma13071562

22. Shahbazi Farahani F, Mecheri B, Reza Majidi M et al (2018) MnOx-based electrocatalysts for enhanced oxygen reduction in microbial fuel cell air cathodes. J Power Sources 390:45–53. https://doi.org/10.1016/j.jpowsour.2018.04.030

23. Liu W, Zheng L, Cheng S et al (2020) Cobalt-nitrogen-carbon nanotube co-implanted activated carbon as efficient cathodic oxygen reduction catalyst in microbial fuel cells. J Electroanal Chem 876:114498. https://doi.org/10.1016/j.jelechem.2020.114498

24. Toyama Y, Miyake K, Shu Y et al (2020) Solvent-free synthesis of Fe/N doped hierarchal porous carbon as an ideal electrocatalyst for oxygen reduction reaction. Mater Today Energy 17:100444. https://doi.org/10.1016/j.mtener.2020.100444

25. Wan J, Deng HP, Shi J et al (2014) Synthesized magnetic manganese ferrite nanoparticles on activated carbon for sulfamethoxazole removal. Clean - Soil Air Water 42:1199–1207. https://doi.org/10.1002/clen.201300432

26. Ai L, Huang H, Chen Z et al (2010) Activated carbon/CoFe2O4 composites: facile synthesis, magnetic performance and their potential application for the removal of malachite green from water. Chem Eng J 156:243–249. https://doi.org/10.1016/j.cej.2009.08.028

27. Zhang G, Qu J, Liu H et al (2007) CuFe2O4/activated carbon composite: a novel magnetic adsorbent for the removal of acid orange II and catalytic regeneration. Chemosphere 68:1058–1066. https://doi.org/10.1016/j.chemosphere.2007.01.081

28. Shao L, Ren Z, Zhang G, Chen L (2012) Facile synthesis, characterization of a MnFe2O4/activated carbon magnetic composite and its effectiveness in tetracycline removal. Mater Chem Phys 135:16–24. https://doi.org/10.1016/j.matchemphys.2012.03.035

29. Shanmugavel T, Raj SG, Kumar GR, Rajarajan G (2014) Synthesis and structural analysis of nanocrystalline MnFe2O4. Phys Procedia 54:159–163. https://doi.org/10.1016/j.phpro.2014.10.053

30. Tyagi A, Penke YK, Sinha P et al (2021) ORR performance evaluation of Al-substituted MnFe2O4/ reduced graphene oxide nanocomposite. Int J Hydrogen Energy 46:22434–22445. https://doi.org/10.1016/j.ijhydene.2021.04.074

31. Rojas-Carbonell S, Santoro C, Serov A, Atanassov P (2017) Transition metal-nitrogen-carbon catalysts for oxygen reduction reaction in neutral electrolyte. Electrochem commun 75:38–42. https://doi.org/10.1016/j.elecom.2016.12.011

32. Kodali M, Santoro C, Serov A et al (2017) Air breathing cathodes for microbial fuel cell using Mn-, Fe-, Co- and Ni-containing platinum group metal-free catalysts. Electrochim Acta 231:115–124. https://doi.org/10.1016/j.electacta.2017.02.033

33. Jiang X, Gu J, Bai X et al (2009) The influence of acid treatment on multi-walled carbon nanotubes. Pigment Resin Technol 38:165–173. https://doi.org/10.1108/03699420910957024

34. Guan D, Gao Z, Yang W et al (2013) Hydrothermal synthesis of carbon nanotube/cubic Fe3O4 nanocomposite for enhanced performance supercapacitor electrode material. Mater Sci Eng B Solid-State Mater Adv Technol 178:736–743. https://doi.org/10.1016/j.mseb.2013.03.010

35. Jayanthi SA, Sukanya D, Pragasam AJA, Sagayaraj P (2013) The influence of peg 20,000 concentration on the size control and magnetic properties of functionalized bio-compatible magnetic nanoparticles. Der Pharma Chem 5:90–102

36. Taufik A, Saleh R (2017) Synthesis of iron(II, III) oxide/zinc oxide/copper(II) oxide (Fe3O4/ZnO/CuO) nanocomposites and their photosonocatalytic property for organic dye removal. J Colloid Interface Sci 491:27–36. https://doi.org/10.1016/j.jcis.2016.12.018

37. Gupta AK, Curtis ASG (2004) Lactoferrin and ceruloplasmin derivatized superparamagnetic iron oxide nanoparticles for targeting cell surface receptors. Biomaterials 25:3029–3040. https://doi.org/10.1016/j.biomaterials.2003.09.095

38. Shi C, Ullah S, Li K et al (2020) Low-temperature synthesis of ultrasmall spinel MnxCo3-xO4 nanoparticles for efficient oxygen reduction. Chinese J Catal 41:1818–1825. https://doi.org/10.1016/S1872-2067(20)63624-5

39. Yan XY, Tong XL, Zhang YF et al (2012) Cuprous oxide nanoparticles dispersed on reduced graphene oxide as an efficient electrocatalyst for oxygen reduction reaction. Chem Commun 48:1892–1894. https://doi.org/10.1039/c2cc17537a

40. Sam S, Nesaraj AS (2011) Preparation of MnFe2O4 nanoceramic particles by soft chemical routes. Int J Appl Sci Eng 9(4):223–239

41. Pal M, Rakshit R, Mandal K (2014) Surface modification of MnFe2O4 nanoparticles to impart intrinsic multiple fluorescence and novel photocatalytic properties. ACS Appl Mater Interfaces 6:4903–4910. https://doi.org/10.1021/am405950q

42. Silambarasu A, Manikandan A, Balakrishnan K et al (2018) Comparative study of structural, morphological, magneto-optical and photo-catalytic properties of magnetically reusable spinel MnFe 2 O 4 nano-catalysts. J Nanosci Nanotechnol 18:3523–3531. https://doi.org/10.1166/jnn.2018.14669

43. Hong D, Yamada Y, Nagatomi T et al (2012) Catalysis of nickel ferrite for photocatalytic water oxidation using [Ru(bpy)3]2+ and S2O82-. J Am Chem Soc 134:19572–19575. https://doi.org/10.1021/ja309771h

44. Jia M, Cheng C, Cui L et al (2020) The effects of deposition time and current density on the electrochemical performance of flexible and high-performance MnO2@PFG composite electrodes. RSC Adv 10:3544–3553. https://doi.org/10.1039/c9ra07682d

45. Zhang H-J, Geng J, Cai C et al (2021) Effect of doping order on metal-free heteroatoms dual-doped carbon as oxygen reduction electrocatalyst. Chinese Chem Lett 32:745–749. https://doi.org/10.1016/j.cclet.2020.05.002

46. Chinnadurai D, Rajendiran R, Selvaraj AR et al (2020) Interplay between porous texture and surface-active sites for efficient oxygen reduction reactions in N-inherited carbon. New J Chem 44:10911–10917. https://doi.org/10.1039/d0nj00841a

47. Ma J, Shi M, Hoang TKA et al (2020) A facile preparation of nitrogen-doped porous carbons from renewable as efficient catalysts for oxygen reduction reaction. J Solid State Chem 291:121609. https://doi.org/10.1016/j.jssc.2020.121609

48. Choi YJ, Mohamed HO, Park SG et al (2020) Electrophoretically fabricated nickel/nickel oxides as cost effective nanocatalysts for the oxygen reduction reaction in air-cathode microbial fuel cell. Int J Hydrogen Energy 45:5960–5970. https://doi.org/10.1016/j.ijhydene.2019.05.091

49. Lee SM, Lalhmunsiama CS, Il TD (2013) Manganese and iron oxide immobilized activated carbons precursor to dead biomasses in the remediation of cadmium-contaminated waters. Environ Sci Pollut Res 20:7464–7477. https://doi.org/10.1007/s11356-013-1609-x

50. Kim A, Muthuchamy N, Yoon C et al (2018) MOF-derived cu@cu2O nanocatalyst for oxygen reduction reaction and cycloaddition reaction. Nanomaterials 8:1–13. https://doi.org/10.3390/nano8030138

51. Mahmoud SA, Bendary SH, Atia H, Martin A (2017) Effect of different electrolytes on the efficiency of dye sensitized solar cells for solar energy conversion. J Nanosci Nanotechnol 17:3719–3728. https://doi.org/10.1166/jnn.2017.14004

52. Mahmoud SA, Mohamed BS, Killa HM (2021) Synthesis of different sizes TiO2 and photovoltaic performance in dye-sensitized solar cells. Front Mater 8:1–11. https://doi.org/10.3389/fmats.2021.714835

53. Lin S, Qiao Q, Chen X et al (2020) Transition metal atom doped C2N as catalyst for the oxygen reduction reaction: a density functional theory study. Int J Hydrogen Energy 45:27202–27209. https://doi.org/10.1016/j.ijhydene.2020.07.103

54. Tian X, Zhou M, Li M et al (2018) Nitrogen-doped activated carbon as metal-free oxygen reduction catalyst for cost-effective rolling-pressed air-cathode in microbial fuel cells. Fuel 223:422–430. https://doi.org/10.1016/j.fuel.2017.11.143

55. Zhang Y, Zhang W, Shen S et al (2017) Sacrificial template strategy toward a hollow LiNi1/3Co1/3Mn1/3O2 nanosphere cathode for advanced lithium-ion batteries. ACS Omega 2:7593–7599. https://doi.org/10.1021/acsomega.7b00764

56. Balasubramanian P, Bin HS, Jansirani A et al (2021) Engineering of oxygen vacancies regulated core-shell N-doped carbon@NiFe2O4 nanospheres: a superior bifunctional electrocatalyst for boosting the kinetics of oxygen and hydrogen evaluation reactions. Chem Eng J 405:126732. https://doi.org/10.1016/j.cej.2020.126732

57. Sidorov SN, Bronstein LM, Davankov VA et al (1999) Cobalt nanoparticle formation in the pores of hyper-cross-linked polystyrene: control of nanoparticle growth and morphology. Chem Mater 11:3210–3215. https://doi.org/10.1021/cm990274p

58. Sharma VK, Waldner F (1977) Superparamagnetic and ferrimagnetic resonance of ultrafine Fe 3O4 particles in ferrofluids. J Appl Phys 48:4298–4302. https://doi.org/10.1063/1.323418

59. Van Santen RA, Tranca I, Hensen EJM (2015) Theory of surface chemistry and reactivity of reducible oxides. Catal Today 244:63–84. https://doi.org/10.1016/j.cattod.2014.07.009

60. Vaidyanathan G, Sendhilnathan S (2008) Characterization of Co1-xZnxFe2O4 nanoparticles synthesized by co-precipitation method. Phys B Condens Matter 403:2157–2167. https://doi.org/10.1016/j.physb.2007.08.219

61. Dung NQ, Duong TTT, Lam TD et al (2019) A simple route for electrochemical glucose sensing using background current subtraction of cyclic voltammetry technique. J Electroanal Chem 848:113323. https://doi.org/10.1016/j.jelechem.2019.113323

62. Fan Z, Li J, Yang W et al (2020) Green and facile synthesis of iron oxide nanoparticle-embedded N-doped biocarbon as an efficient oxygen reduction electrocatalyst for microbial fuel cells. Chem Eng J 385:123393. https://doi.org/10.1016/j.cej.2019.123393

63. Xiao Z, Ning G, Yu Z (2019) MnO@graphene nanopeapods derived via a one-pot hydrothermal process for a high performance anode in Li-ion batteries. Nanoscale 11:8270–8280. https://doi.org/10.1039/c8nr10294e

64. Duan J, Zheng Y, Chen S et al (2013) Mesoporous hybrid material composed of Mn3O4 nanoparticles on nitrogen-doped graphene for highly efficient oxygen reduction reaction. Chem Commun 49:7705–7707. https://doi.org/10.1039/c3cc43338b

65. Khater DZ, Amin RS, Mahmoud M, El-Khatib KM (2022) Evaluation of mixed transition metal (Co, Mn, and Cu) oxide electrocatalysts anchored on different carbon supports for robust oxygen reduction reaction in neutral media. RSC Adv 12:2207–2218. https://doi.org/10.1039/d1ra07721j

66. Ortiz-Martínez VM, Touati K, Salar-García MJ et al (2019) Mixed transition metal-manganese oxides as catalysts in MFCs for bioenergy generation from industrial wastewater. Biochem Eng J 151:107310. https://doi.org/10.1016/j.bej.2019.107310

67. Roche I, Scott K (2009) Carbon-supported manganese oxide nanoparticles as electrocatalysts for oxygen reduction reaction (orr) in neutral solution. J Appl Electrochem 39:197–204. https://doi.org/10.1007/s10800-008-9653-9